nature reviews methods primers

https://doi.org/10.1038/s43586-025-00425-8

Supplementary information

Time-domain thermoreflectance

In the format provided by the authors and unedited

Supplementary Information for

Time Domain Thermoreflectance

Ramya Mohan,[1*] Samreen Khan,[2*] Richard B. Wilson,[2,3] Patrick E. Hopkins[1,4,5**]**

1. Dept. of Mechanical and Aerospace Engineering, University of Virginia, Charlottesville, VA

2. Dept. of Mechanical Engineering, University of California, Riverside, CA

3. Materials Science and Engineering Program, University of California, Riverside, CA

4. Dept. of Materials Science and Engineering, University of Virginia, Charlottesville, VA

5. Dept. of Physics, University of Virginia, Charlottesville, VA

*equal contributions

**authors to whom correspondence should be addressed:
rwilson@ucr.edu, phopkins@virginia.edu

Supplementary Box 1:

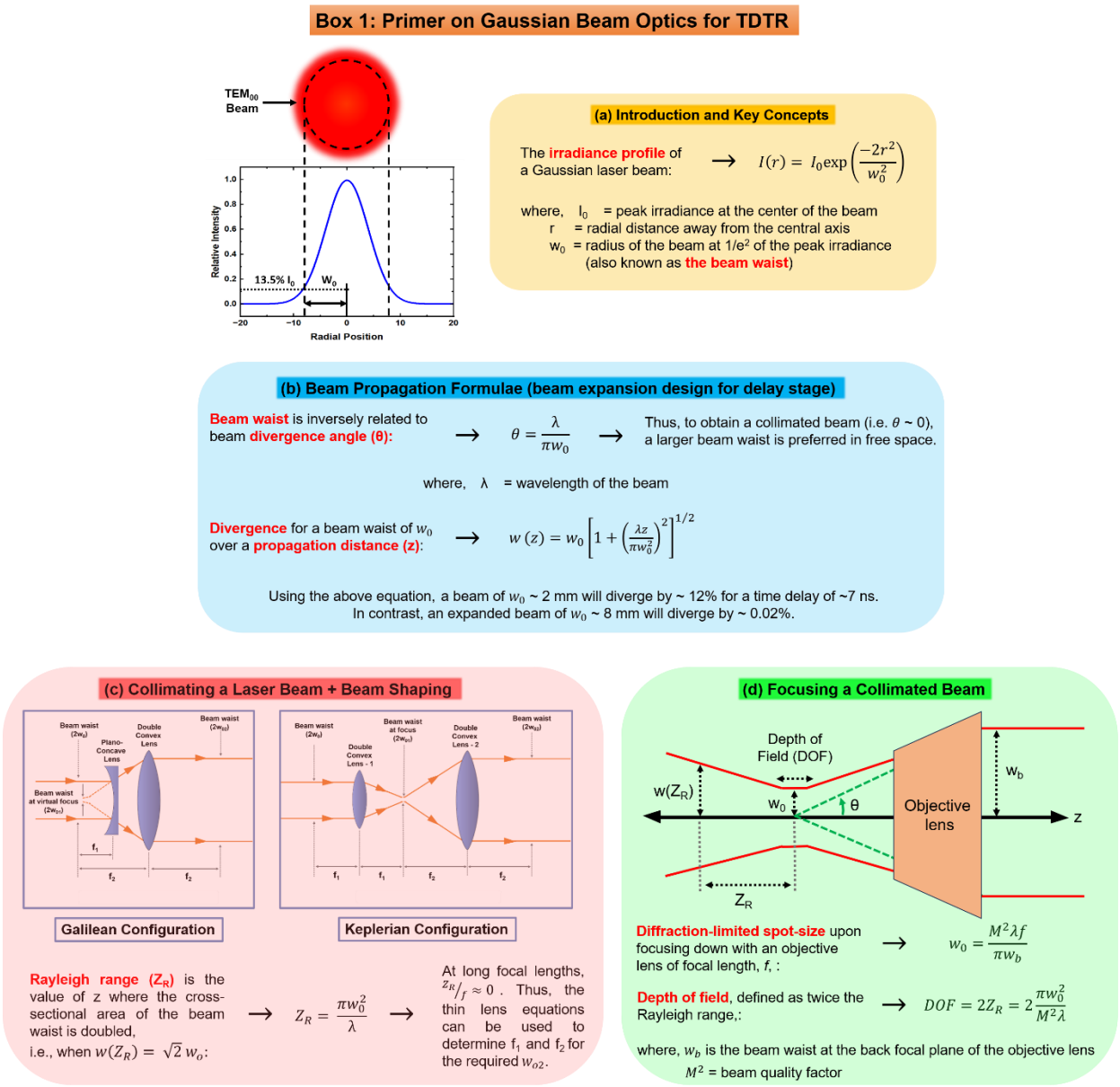

Supplementary Box 1: A Primer on Gaussian Beam Optics for TDTR. We present a short guide to the relevant beam optics when working with beam propagation and beam shaping across a TDTR setup. We first introduce the basic concept of a Gaussian beam; which can be completely described using its beam waist, divergence angle, and irradiance profile. Next, we provide formulae to determine the beam divergence for a given beam waist (i.e., $1/e^2$ spot size), which is crucial to determine how much a beam needs to be expanded before it is passed through a delay stage, to ensure minimum beam divergence and/or wander. We also provide a introduction into the concept of Rayleigh ranges, and demonstrate how to collimate a beam using two standard configurations: the Galilean and Keplerian configurations. Depending on how much table space is available, either of these configurations could be utilized to steer and collimate a beam. Finally, a guide on how to determine the $1/e^2$ spot size at focus is provided (i.e., what is the diffraction-limited spot size possible for a given beam waist in free space). This also aids in determining the M^2 factor of a laser beam off the oscillator.

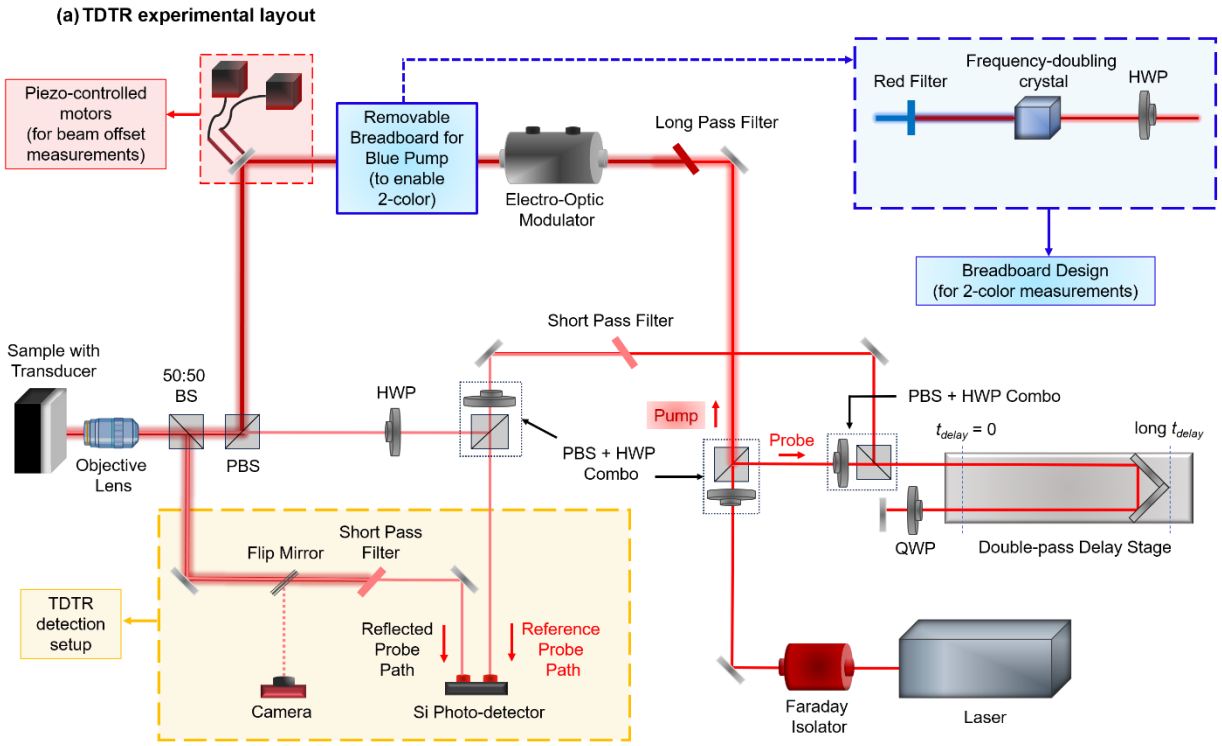

Figure S1. Detailed TDTR layout, with a balanced detection scheme to attenuate laser intensity noise, optical filters for pump beam rejection (two-tint system), or a frequency-doubling system for the pump beam (two-color system).

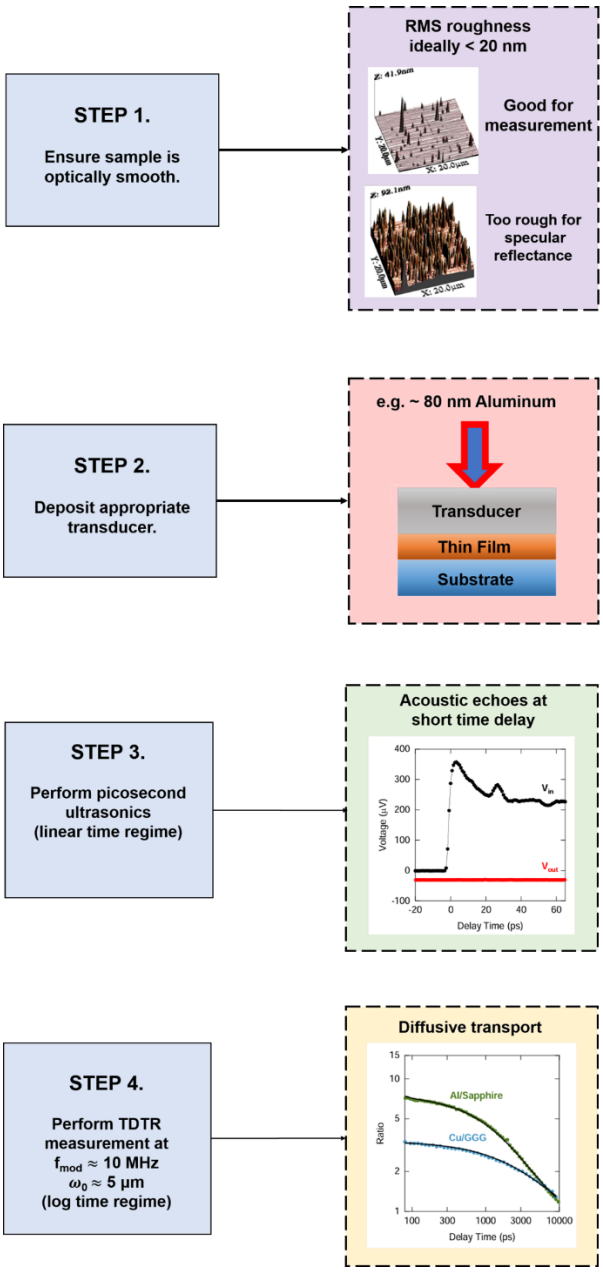

Figure S2. A Four-Step Standard Operating Protocol (SOP) for Standard TDTR Measurements Step 1. involves sample surface characterization to ensure an optically smooth film. We show AFM (atomic force microscopy) images of two sample surfaces – the top sample surface is smooth with a few point defects, suitable for TDTR measurements; the bottom sample surface is rougher and will not yield specularly reflecting beams for a TDTR measurement [1]. A good rule of thumb is to ensure that the rms surface roughness is < 20 nm (or ~λ/40, where λ = pump/probe wavelength). Step 2. involves the deposition of an appropriate transducer – the most commonly used transducer is Aluminum, with a targeted thickness of ~ 80 nm. 4 probe electrical resistivity measurements can be used to characterize the film quality and obtain the thermal conductivity of the transducer. Step 3. involves picosecond ultrasonics measurements to measure the thickness of the deposited transducer, where the acoustic echoes in the phase-corrected Vin signal at short time delay are utilized on an Al/Sapphire sample [2]. Step 4. involves the TDTR measurement at high modulation frequencies (e.g., ~ 10 MHz) and large spot sizes (e.g., 5 μm) to determine k_z and G as a function of pump-probe delay time in Al/sapphire and Cu/GGG (where Cu is the transducer) [2].

Supplementary Table 1:

Technique	Working Principle	Advantages	Limitations/Challenges	Critical Requirements
TDTR	Thermo-reflectance	- Reliable non-contact method to measure k and G across a wide variety of bulk and thin film samples	- Transducer needs to be optically opaque; thus, limiting K and G measurements - Use of high-k thick transducer is severely limiting when measuring in-plane thermal conductivity, especially in thin films - Cannot resolve G when the Kapitza length is less than the transducer thickness (i.e., 80 nm) - Probes only the near surface volume between 100 nm and 10 microns, depending on *k/C*.	- Samples must be specularly smooth (<10 nm). - The transducer must be completely opaque (i.e., the thickness must be 70 – 100 nm)
TR-MOKE	Magneto-optic Kerr Effect	- Use of optically semi-transparent transducer aids in greater sensitivity to both k and G - This technique is particularly useful in k_r measurements of thin films - Could possibly be more forgiving of rough sample	- Difficult to obtain a magnetic transducer with PMA - Determining the thickness of a Co-Pt multilayer transducer stack is challenging - The magnetization of the sample can deteriorate over time.	- Transducer should have low M_s (saturation magnetization) or large perpendicular magnetic anisotropy so it's easy to orient M out-of-plane.

		surfaces on account of +/- field measurements - Less noisy data on account of +/- field measurements	- Measurement with ultrathin transducers < 10 nm are sensitive to *C* of adsorbed molecules from air.	
Beam Offset	Non-concentric beams (can do both TDTR-BO and TR-MOKE BO)	- Usually insensitive to cross-plane conductances in a sample stack; thus, can provide an in-plane k measurement with minimal uncertainty propagation from G and k_z.	- Challenging to measure in-plane k in conductive thin films - Phase jitters at low modulation frequencies lead to significant uncertainties in k_r - Extremely sensitive to spot-size	- Must accurately determine the correlation factor between movement of the mirror/goniometer in radians and the beam offset translation distance on the sample in micrometers.
Laser Flash	Cross-plane separation of heating and temperature sensing.	- Provides a measure of spatiotemporal profile of temperature in cross-plane direction.	- Requires a transducer on both sides of the sample, and sample has to be thin, e.g. 0.1 to 10 microns, depending on *k/C*.	- Requires optically opaque transducers
SSTR	Steady state thermo-reflectance	- Affords greater penetration depths of thermal waves in the sample, thus, allowing for buried interfaces, etc. to be measured. - Does not require requisite knowledge of heat capacity of the sample	- Must accurately characterize the scaling factor correlating the power deposited onto the sample with ΔT.	- Requires optically opaque transducers

Supplementary Note 1: Detector, Detector Circuit and RF lock-in Considerations

Spectral Separation of Pump and Probe Beams. To prevent both specular and diffuse reflections of the pump light from reaching the detector, TDTR setups use spectral separation techniques. This can be achieved using either a two-tint configuration[3] (filters in Fig. S1) where steep-edged filters are employed, or, a two-color configuration where the pump beam is frequency doubled with a BiBO or β-BBO crystal (bread board apparatus in Fig. S1).

A two-tint setup takes advantage of the fact that a ~100 fs laser pulse has a spectral width on the order of 10 nm. Let's assume the center wavelength of the laser is 785 nm, so the laser's power is at wavelengths between 780 and 790nm. A long pass optical filter red-shifts one of the beams (pump beam in Figure S1), by blocking transmission less than some cutoff wavelength, e.g. 787 nm. A short-pass filter blue-shifts the other beam (probe beam in Figure S1) by blocking transmission of power at wavelengths greater than some cutoff wavelength, e.g. 783 nm. Then, the same filter that is on the probe path is placed in front of the detector. In Fig. S1, this is a short pass filter. Since the pump is red-shifted to wavelengths longer than 787 nm, it is blocked, as the short-pass filter blocks power at wavlelengths longer than 783 nm.

A frequency doubled system works similarly. But it uses a single long pass filter on the detector line to block the frequency-doubled pump beam.

By spectrally narrowing the beams, the two-tint configuration broadens the laser pulses to the order of ~1 ps [4].

A down side of spectral separation of the pump and probe beams is there is significant power lost. With the two-tint configuration described in Ref. [4], the pump and probe filters each attenuate the pump and probe power by a factor of 3-4. The attenuation, and filtering efficiency, depends on the filters' cut-off wavelengths. These wavelengths can be tuned slightly by tilting the filters. In power limited experiments, increasing transmitted power by adjusting the filter tilt is beneficial. However, this makes the detector filter less effective at rejecting pump light. Therefore, in these experiments, it is necessary to rely more heavily on spatial and polarization filtering of the pump beam.

For setups employing frequency doubling, power losses are similarly substantial. Typical conversion efficiencies are only 5-10%.

Modulation of the Pump Beam and the RF-lock in. Since achieving the necessary polarization change requires large voltage swings, the EOM is connected to a dedicated driver that amplifies an input signal from a function generator. The driver's bias and driving voltage need to be set to optimize the depth of modulation.

TDTR requires the pump beam induce a thermal response at f_{mod}. To accomplish this, the pump beam can be modulated using either a harmonic or square wave form. The harmonic response at f_{mod} is quantity of interest. However, using a square waveform is acceptable. Square wave heating generates thermal responses at odd harmonics of f_{mod}. Responses at higher order harmonics (3 f_{mod} and above) can by filtered with a digital RF lock-in, e.g., Zurich. Alternatively, an analog lock-in, e.g. the SRS 844, mixes the measured signals with a square-wave at f_{mod}. In this case, unwanted higher-order harmonics must be filtered before lock-in amplification. The higher-order harmonics can be removed with a simple bandpass filter or lowpass filter in the detection circuit.

It is sometimes desirable to measure the thermal response at multiple heating frequencies. Digital lock-ins allow demodulation of multiple frequencies at once.

Since either harmonic and square-wave modulation is suitable for TDTR experiments, the decision about which is best is related to cost and performance of accompanying dedicated driver. For example, the Conoptics 350-160 EOM is commonly used in TDTR systems. It can be driven by an analog driver (model 25A) that can produce a harmonic waveform, or a digital driver (model 25D) that produces a square wave. The digital driver has superior modulation amplitude and bandwidth at a similar cost, therefore many TDTR systems implement a square wave modulation scheme.

Detector. Si photodetectors are operational at wavelengths of ~ 400 – 1000 nm, and feature excellent responsivity at a wavelength of ~800 nm, and thus, are heavily used in TDTR detection set-ups. The reflected probe beam should be focused to a spot much smaller than the detector's active area to avoid clipping, e.g., less than half the detectors area. It should not be focused to such a small area, e.g. tens of microns, that detector nonlinearities are an issue.

Many TDTR setups use a simple Si photodiode. However, balanced detection can reduce noise caused by laser power fluctuations by balancing the signal with a reference beam that does not interact with the sample. This is particularly useful when preforming experiments at low

modulation frequencies, which allows for measurements of thermal diffusivity [5]. When utilizing such a balanced photodetection setup, both the probe beams must be focused down to the same spot-size at the aperture, or detector non-linearities hinder common mode rejection of the noise. The path length of the reference beam and reflected probe beam should also be the same (or at least similar) to optimize common mode rejection.

Step-by-step guide for building TDTR setups. We recommend that the laser beam from the Ti:sapphire oscillator be centered around a wavelength of either ~808 nm or ~785 nm. This is particularly important when designing a 2-tint TDTR setup, because most steep-edged filters are designed to operate around those wavelengths (purchase of optical filters recommended from Semrock, Edmund Optics). Beams at other wavelengths, such as at ~800 nm can be challenging to spectrally separate into low-pass and high-pass configurations, and may require specially designed steep-edged filters, with significant power attenuation.

The laser beam must then be passed through a Faraday Isolator in order to prevent any accidental back-reflections from destabilizing the laser cavity. The laser beam must ideally feature a circular Gaussian profile. If the beams are elliptical, then a pair of cylindrical lenses must be employed to make the beams spherical in free-space. The laser light is then passed through a half-wave-plate (HWP) and polarized beam splitter (PBS) optics pair, where it is separated by polarization into a high-intensity pump and a low-intensity probe beam. The relative intensities of the pump and probe are controlled by rotating the half-wave-plate.

The probe beam path: In our schematic, the probe beam is time-delayed with respect to the pump beam, by passing it through a mechanical delay stage in a two-pass configuration (as shown in the schematic in Fig. 2 in the main document and Fig. S1). A two-pass configuration allows for the correction of any divergence and/or beam wander along the delay stage. In certain other setups, the pump beam is time-advanced with respect to the probe beam, and this allows for lesser artifacts in the signal on account of spot-size changes and/or beam wander as a function of delay time. However, care must be taken to account for the phase-heating function in the measured V_{in} and V_{out} signals, when advancing the pump (details are provided in the Experimentation Section of the main document). Next, the probe beam is sent through a short-pass optical filter, where wavelengths > 785/808 nm are filtered, and only shorter wavelengths are allowed to transmit. This results in a power loss of up to 55%.

The pump beam path: The pump beam is modulated at a desired frequency by passing it through an electro-optic modulator (EOM). Aligning the pump beam through the EOM is absolutely crucial, and will directly impact the quality of data obtained, especially at low modulation frequencies (< 1 MHz). Detailed instructions on how to align the EOM are provided in both the Conoptics resource guide, as well as in online tutorials by Prof. Joseph Feser, and we recommend that the user familiarize themselves with both these resources. To summarize alignment through the EOM, the pump beam must be converged and collimated using a pair of collimating lens such that it is small enough to enter the narrow aperture of the EOM (beam diameter < ~2 mm). Next, a half-wave-plate (HWP) placed before the EOM, will ensure that the polarization of the beam is optimized for maximum modulated transmittance at 50% EOM duty cycle, without having to rotate the EOM itself. Rotating the EOM can sometimes cause a distortion in the beam shape, resulting in an elliptical pump beam. A function generator is used to send a square-waveform to the EOM ($0 \leq f_{mod} \leq 20$ MHz), while certain setups also utilize a sinusoidal waveform to modulate the beam. A well aligned pump beam through the EOM will feature at least ~45% modulated transmission, and will be spherical in free-space. The pump beam is then sent through a long-pass optical filter, where wavelengths < 785/808 nm are filtered, and only longer wavelengths are allowed to transmit. This results in a power loss of up to 65%. We recommend using optical filters with AR-coatings (anti-reflective coatings), to prevent stray back-reflected beams from causing signal artifacts in the final data.

Pump/Probe beams at the sample stage: The pump and probe beams must be well-collimated before they are focused down onto the sample surface using infinity-corrected long-working distance objective lens. A portion of the reflected pump/probe beams can be directed onto a camera to image the surface of the sample (an extensive summary of beam-sample interactions is provided in the Experimentation section of the main document).

Reflected probe beam at the detector: The pump and probe beams are both reflected from the sample surface, however, a TDTR experiment only utilizes thermoreflectance signals from the reflected probe beam. The pump beam must therefore, be completely rejected, through means of either a band-pass filter (in a 2-tint setup) or a blue filter (in case, the pump beam is frequency-doubled in a 2-color setup). The probe beam is then focused down to the aperture of a balanced Si photodetector, using a long-distance focal lens. An additional “reference” probe beam, that doesn’t

interact with the sample, is sent through another long-distance focal lens (with the same focal length as that in the reflected probe beam path) to the other aperture of the photodetector. The resulting RF (radio frequency) voltage signal sent to the RF-lock-in amplifier will feature enhanced SNR (signal to noise ratio) on account of the noise suppression because of this balanced detection scheme.

Supplementary Note 2: Signal Theory and Choosing a pump modulation frequency

Signal Theory. To gain a physical intuition for the in-phase and out-of-phase signals in a TDTR experiment, its useful to compare the TDTR thermal response to the response of simpler heating functions. We examine how the temperature response from TDTR's harmonically modulated train of pump pulses compares to simpler heating scenarios. Specifically, we contrast it with the response to a single laser pulse and to purely harmonic heating.

After absorbing a single laser pulse, the metal transducer's initial temperature rise is determined by the volume over which the laser pulse energy is spread, and the transducer's heat-capacity per unit volume C_m. Then, heat-decays into the sample on a time-scale τ:

$$\Delta T_1(t) = \frac{A_0}{\pi w_0^2 h}\frac{1}{C_t} f(-t/\tau) \qquad \text{(S2.1)}$$

where A_0 is the pulse energy absorbed by the transducer, w_0 is the 1/e^2 spot size, and h is the thickness of the transducer. Here, $f(-t/\tau)$ describes the decay of the sample after heating and depends on τ, k, and C.

For high thermal conductivity materials ($k > hG$, where k is the thermal conductivity and G is the interface conductance), the rate at which the transducer's temperature decays is primarily determined by G and heat-capacity per unit area: $\tau = hC_t/G$, and $f(-t/\tau) = \exp(-t/\tau)$. For low thermal conductivity materials ($k < hG$) the decay of the transducer's temperature is limited by the ability of the sample to carry heat away from the transducer/sample interface, and thus, τ is determined by the thermal properties of the substrate.

The thermal response of a 1D semi-infinite solid to harmonic heating at a frequency f, $q(t) = q_f \exp(i2\pi f t)$, is

$$\Delta T_h(t) = \Delta\bar{T}(f)\exp(i2\pi f t), \text{ with } \Delta\bar{T}(f) = \frac{q_f}{2\sqrt{k\pi C f}}(1-i). \qquad \text{(S2.2)}$$

By defining the thermal penetration depth to be $d_p = \sqrt{k/\pi C f}$, it can be seen that Eq. (S2.2) has the familiar form of the thermal version of Ohm's law: ΔT is proportional to the product of the heat-current q_f and thermal resistance d_p/k. We also see that that the temperature response lags the heating function by $\pi/4$ because the amplitude of the in-phase and out-of-phase responses are equal.

The in-phase and out-of-phase temperatures measured in a TDTR experiment caused by heating from a modulated train of pump pulses are constructed from the frequency-domain response of the sample to harmonic heating [1]:

$$\Delta T_{in}(t) = \frac{1}{2}\sum_{m=-\infty}^{\infty}[\Delta\bar{T}(mf_{rep} + f_{mod}) + \Delta\bar{T}(mf_{rep} - f_{mod})]\exp(i2\pi m f_{rep} t), \quad \text{(S2.3)}$$

$$\Delta T_{out}(t) = -\frac{i}{2}\sum_{m=-\infty}^{\infty}[\Delta\bar{T}(mf_{rep} + f_{mod}) - \Delta\bar{T}(mf_{rep} - f_{mod})]\exp(i2\pi m f_{rep} t). \quad \text{(S2.4)}$$

In Fig. S3(a), we show the thermal response of a Cu crystal coated with an Al thin-film transducer to the three types of heating. For this calculation, the laser spot size is set to $w_0 \approx 10$ μm, which is large enough to ensure that heat transfer is one-dimensional in the through-plane direction. This is because the in-plane temperature gradient scales with $1/w_0$, while the through-plane gradient scales with $1/d_p$, so the through-plane heat-current dominates. The interface conductance is set to 135 MW m^{-2} K^{-1}. The pump modulation frequency to $f_{mod} = 1/8\, f_{rep} = 10$ MHz, a choice that minimizes the effects of pulse accumulation in the in-phase signal (discussed more in Supplementary Note 4). Finally, we set $q_f = A_0 f_{rep}/\pi w_0^2$

Figure S3(a) shows that the in-phase signal measured by the RF lock-in a TDTR experiment is, primarily, a measure of the sample's thermal response to a single laser pulse. Alternatively, the out-of-phase signal measured by the RF lock-in is, primarily, a measure of the out-of-phase response to harmonic heating with $f = f_{mod}$. The in-phase signal corresponds to the temperature response synchronized (in-phase) with the pump modulation. It reflects the immediate temperature rise and the energy stored in the sample after each pump pulse. In contrast, the out-of-phase signal lags the pump by 90° and captures the delayed thermal response governed by heat diffusion away from the heated region. The sample acts as a thermal integrator. Energy is deposited in discrete pulses but diffuses away slowly. Over time, the integrated response is similar to that from continuous harmonic heating.

The curves for the single-pulse response vs. TDTR response in Fig. S3(a) deviate at short delay times, since Eq. (S2.1) neglects the time required for the transducer to thermalize **[G]**. At long delay times, Eq. (S2.1) over-estimates the decay rate slightly because it does not include the effect of heat accumulation (temperature rise) at the surface of the substrate. However, the deviation is small, indicating that the time-domain response of the sample has little sensitivity to the Cu's

thermal conductivity. The harmonic response, $Im\left(\Delta\bar{T}(f)\right)$, is also in good agreement with ΔT_{out}, at least at short-delay times.

Mathematically, this result is straightforward to understand by considering the convergence of the series in Eq. (S2.3) and (S2.4) near $t = 0$. For $t \approx 0$, $\exp(i2\pi m f_{rep} t) \approx 1$. Grouping the $+m$ and $-m$ terms in the series, and invoking the identities $\Delta T(f) - \Delta T(-f) = 2i \cdot \mathrm{Im}(\Delta T(f))$ and $\Delta T(f) + \Delta T(-f) = 2 \cdot \mathrm{Re}(\Delta T(f))$, we obtain

$$\Delta T_{in}(t \approx 0) = (Re[\Delta T(f_{mod})]) + \sum_{m=1}^{\infty}\left(\mathrm{Re}\left[\Delta T\left(m f_{rep} + f_{mod}\right)\right] + \mathrm{Re}\left[\Delta T\left(m f_{rep} - f_{mod}\right)\right]\right), \quad \text{(S2.5)}$$

$$\Delta T_{out}(t \approx 0) = -(Im[\Delta T(f_{mod})]) - \sum_{m=1}^{\infty}\left(\mathrm{Im}\left[\Delta T\left(m f_{rep} + f_{mod}\right)\right] - \mathrm{Im}\left[\Delta T\left(m f_{rep} - f_{mod}\right)\right]\right). \quad \text{(S2.6)}$$

Since $\Delta T(f)$ scales as $1/\sqrt{f}$, the $m \geq 1$ terms in T_{in} are individually smaller than the fundamental $\Delta T(f_{mod})$ term yet add constructively, making them collectively significant and accounting for the rapid temporal evolution of the pulsed response. In contrast, the subtractive nature of the series for T_{out} causes high-frequency contributions to nearly cancel. At f_{mod} = 10 MHz, the ΔT_{out} series converges by m=2 with the fundamental term, $Im[\Delta T(f_{mod})]$, comprising roughly 85% of the total. If f_{mod} is decreased, the fundamental term comprises an increasingly greater fraction of T_{out}.

In TDTR experiments, the ratio of the in-phase and out-of-phase response is analyzed. First, we divide Eq. (S2.1) by the imaginary part of Eq. (S2.2). We note that, in a TDTR experiment, $q_f = f_{rep}(A_0/\pi w_0^2)$. Then, we arrive at the following approximation for the ratio signal:

$$-\frac{V_{in}}{V_{out}} = -\frac{T_{in}}{T_{out}} \approx \frac{\Delta T_1(t)}{\mathrm{Im}(\Delta T(f_{mod}))} = \frac{2\sqrt{\pi f_{mod}}}{f_{rep}}\frac{\sqrt{kC}}{hC_t} f(-t/\tau). \quad \text{(S2.7)}$$

This is Eq. 2.2. in the main text. The ratio is proportional to the sample's thermal effusivity, $\sqrt{kC}$, divided by the transducer's heat-capacity per unit area, hC_m. The proportionality constant only depends on the laser repetition rate and modulation frequency, which are precisely known. The dependence on laser powers, sample absorption, and sample thermoreflectance have divided out. Equation S2.7 neglects the effects that G and hC_t have on the out-of-phase signal, which are not negligible. It also neglects the effect of the sample's thermal resistance on the decay of the in-

phase signal, which is significant for low thermal conductivity materials. Therefore, Eq. S2.7 should not be used to analyze data. Data analyses should be performed with the multilayer thermal models described in [6]. Nevertheless, Eq. S2.7 is useful for qualitatively understanding the observed ratio signals.

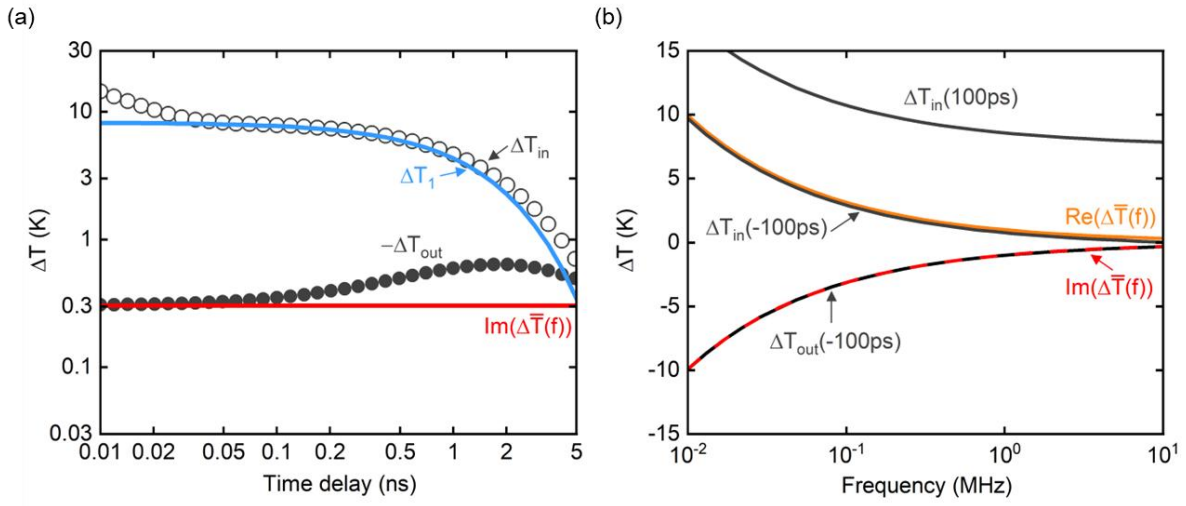

Figure S3: Thermal response in TDTR measurements. (a) Comparison of the in-phase and out-of-phase thermal response in a TDTR experiment, ΔT_{in} and ΔT_{out}, to the expected response for heating by a single pulse, ΔT_1, and harmonic heating, $Im(\Delta\bar{T}(f))$ for a Cu crystal with an Al transducer. (b) Prediction for how the thermal signals in a TDTR experiment, $\Delta T_{in}(-100\ ps)$, $\Delta T_{in}(100\ ps)$, and $\Delta T_{out}(-100\ ps)$, depend on heating frequency f_{mod}. The TDTR signals from pulse accumulation, $\Delta T_{in}(-100\ ps)$ and $\Delta T_{out}(-100\ ps)$, are nearly equal to the response one would expect due to harmonic heating without discrete laser pulses: $\Delta\bar{T}(f)$.

Choosing a Modulation Frequency. In the above discussion of signals, we did not consider the effects of pulse accumulation on the in-phase signal. In Fig. S3(b), the effect of pulse accumulation on ΔT_{in} only appears at delay-times longer than 3 ns, after the pulsed response, $\Delta T_1(t)$, has diminished. The minimal role of pulse accumulation on ΔT_{in} is a consequence of setting $f_{\mathrm{mod}} = 1/8 \cdot f_{rep}$. Fig. S3(c) shows $T_{in}(-100\ ps)$, $T_{in}(100\ ps)$, and $T_{out}(-100\ ps)$. Since ΔT_{out} describes the lagged thermal response of the sample, it is not sensitive to small changes in delay time (i.e., $T_{out}(t = -100\ ps) = T_{out}(t = 100\ ps)$). For simplicity, the calculation in Fig. S3(b) neglects any effects of in-plane transport. Two features in Fig. S3b are notable. First, the change in the in-phase signal: $\Delta T_{in}(100\ ps) - \Delta T_{in}(-100\ ps)$ equals the single pulse response $\Delta T_1(0)$ at all f. So, ΔT_{in} can be viewed as the sum of pulse accumulation (given by $\Delta T_{in}(-100\ ps)$) and the single pulse

response ΔT_1. Second, $T_{in}(-100\ ps)$ crosses through zero at $f_{mod} \approx 1/8 \cdot f_{rep}$. Therefore, choosing $f_{mod} \approx f_{rep}/8$ minimizes pulse accumulation in the in-phase signal.

Minimizing pulse accumulation in ΔT_{in} is advantageous because we want ΔT_{in} to depend primarily on the transducer properties. The reason for this is the following. $\Delta T_{in}(-100\ ps)$which is approximately equal to the real part of the harmonic response at f_{mod}, depends on the sample's thermal properties in the same way as ΔT_{out}. As a result, at low frequencies where $\Delta T_{in}(-100\ ps) > \Delta T_1$, the ratio loses sensitivity to the sample's thermal properties. This is why the default modulation frequency for "standard" TDTR experiments is near 10 MHz, and also (partly) why measurements at low frequencies, e.g., kHz, are uncommon. (The other reason being that laser noise also becomes more problematic at low frequencies.). For many types of measurements, it is advantageous to set the modulation frequency to be much less than $f_{rep}/8$. This adjustment increases the thermal penetration depth, thereby enabling TDTR to determine a variety of thermal properties of samples, such as the in-plane thermal conductivity or heat capacity.

There are two obstacles to low-frequency TDTR measurements. The first is pulse accumulation in the in-phase signal. In some situations, a large value of $\Delta T_{in}(-100\ ps)$ causes the ratio to lose sensitivity to the thermal properties of interest. This can be circumvented by analyzing a modified ratio. The change in ΔT_{in} between -100 and +100 ps will always depend solely on the heat-capacity per unit area of the transducer, regardless of the modulation frequency. Therefore, analyzing $[\Delta T_{in}(t) - \Delta T_{in}(-100\ ps)]/\Delta T_{out}(t)$ instead of $\Delta T_{in}(t)/\Delta T_{out}(t)$ solves this obstacle.

The second obstacle to low-frequency TDTR measurements is noise. Ti:sapphire oscillators become noisy at low-frequencies. The intensity noise can be overcome by using a balanced detection scheme, as illustrated in Fig. S1.

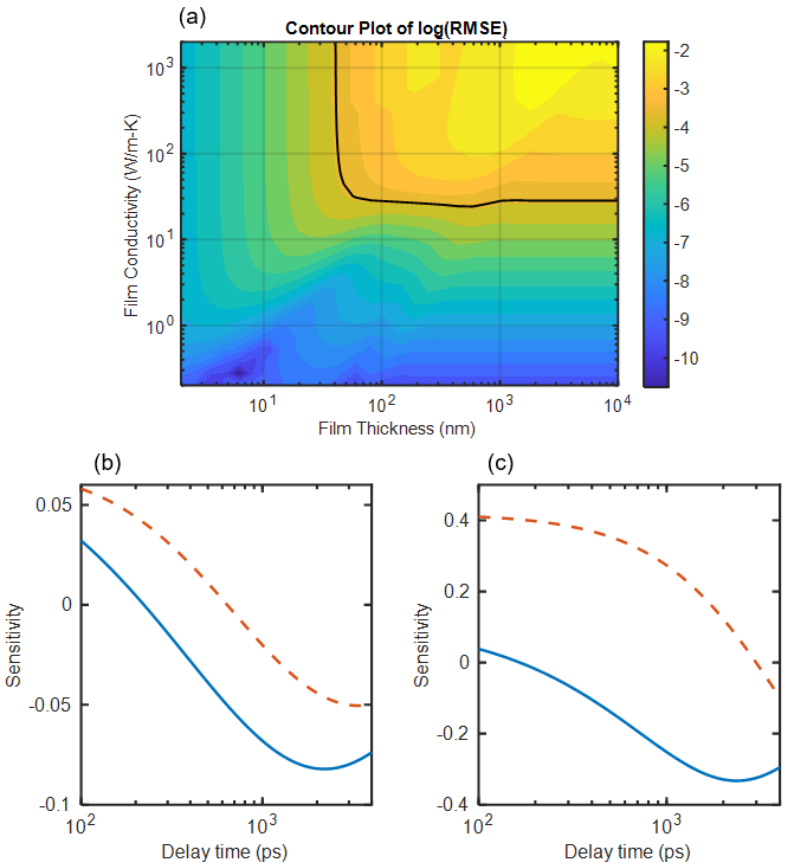

Figure S4: Parameter coupling calculation. These calculations use the TDTR thermal model from Supplementary Ref. 4 to explore whether a TDTR measurement of a thin-film on a silicon substrate can independently determine two parameters: the interface conductance between an 85 nm Al transducer and the thin-film, and thin-film thermal conductivity. The interface conductance was set to 400 MW m^{-2} K^{-1}. (a) Contour map of the natural logarithm of the root-mean-square relative error (RMSE) between the TDTR model and simulated data when the interface conductance is changed to 1.5 × its true value. The bold black contour line marks a 3% error threshold: points below this line (RMSE < 3 %) indicate strong coupling (blue and green), since even with the interface conductance fixed incorrectly, the best-fit thermal conductivity can be adjusted to recover an almost perfect fit (low RMSE). (b) Sensitivity curves for TDTR measurement of a 20 nm film with k = 5 W m^{-1} K^{-1} on silicon. The interface conductance was set to 200 MW m^{-2} K^{-1}. The sensitivity is defined as the fractional change in the ratio due to some fractional change in a thermal model parameter. The solid line is the sensitivity of the ratio vs. delay time to the interface conductance, while the dashed line shows the sensitivity to the film conductivity. The two curves share nearly identical shapes, so changing one parameter can be exactly offset by the other. This indicates the parameters are strongly coupled, and TDTR cannot independently determine them. (c) Sensitivity curves for a 500 nm film with k =30 W m^{-1} K^{-1}. The film conductivity effects the ratio most strongly at short delays, while the interface conductance at long delays. As a result, the two parameters are not coupled, and a TDTR measurement can independently determine both.

Supplementary Note 3: Transducer Considerations and TDTR Without a Transducer

Choosing a Transducer. TDTR experiments usually require coating the sample with a metal transducer. The sample surface before and after transducer deposition needs to be smooth (< 10 nm). The metal transducer in a TDTR experiment serves several purposes. Metals typically have optical penetration depths of 10-20 nm [7]. Therefore, a metal transducer with h_t >50 nm completely confines heating and temperature sensing to the sample's surface. Without a transducer, the laser interacts with the sample over sub-micron or micron scales, depending on the sample's extinction coefficient. A long interaction length makes it hard to resolve nm-scale heat-transfer processes. The transducer also prevents excitation of electron-hole pairs. An opaque transducer also simplifies thermal modeling. Without a transducer, it's necessary to calculate absorption as a function of depth [8]. Additionally, without an opaque transducer, the thermoreflectance signal is a depth-weighted temperature average, not a temperature at one defined location [8,9].

The transducer ensures that heat is evenly spread across the well-defined depth h_t at time delays between ${h_t}^2 C_t/k_t$ and τ. (${h_t}^2 C_t/k_t$ is the time-scale for the transducer to thermalize after laser absorption.) As a result, the only thermal property V_{in} depends on at these time-delays is $h_t C_t$. This feature is fundamental to the operational principle standard TDTR experiments (see Signal Analysis section above). As a result, standard TDTR measurements of the cross-plane k of bulk metals require a transducer (See Supplementary Note X), despite metals having a short optical penetration depth, and no issues with electron-hole pairs.

The following criteria should be considered when selecting the transducer. The figure of merit for maximizing signal-to-noise is $1/R(dR/dT)$ of the metal at the probe wavelength [7,10]. This value typically peaks at wavelengths with interband optical transitions [11]. The transducer resistance $(h/k)$and the transducer/sample boundary resistance $(1/G)$ add to the sample's intrinsic thermal resistances. For cross-plane measurements, h/k and $1/G$ should be small compared to the resistance of interest. For thin-films, the thermal resistance of interest is h_{film}/k_{film}, while for bulk samples its $d_p/k_{substrate}$. The interface conductance G depends on the transducer's bonding strength to the sample, so minimizing $1/G$ means picking a transducer that forms chemical reactions with the sample [12,13]. Minimizing $1/G$ also requires the sample surface be clean prior to transducer deposition, which can be achieved by a RF-sputter etch or pre-deposition bake. Transducers must also be stable. So, its desirable for the transducer to form a self-limiting native

oxide (e.g., Al or Ta), or be inherently inert (e.g., Au or Pt). A large piezo-reflectance coefficient at the probe wavelength is also useful because it enables film-thickness determination by picosecond acoustics. Like dR/dT, piezo-reflectance peaks at interband-transition wavelengths [14].

Aluminum is a good transducer for most experiments with a probe wavelength near 800 nm, where it has large thermoreflectance, strong picosecond acoustic signals, and high k. It also has good adhesion to most samples. For measurements at high T, a refractory metal, e.g. Ta, is a better choice. For high T measurements, it is also a good idea to choose a metal whose thermal expansion coefficient is similar the underlying sample to reduce thermal strain and prevent plastic deformation and delamination.

For TR-MOKE experiments, different factors need to be considered when choosing a transducer. In a TRMOKE experiment, the probe laser reflects from the sample at normal incidence. In this geometry, the probe beam is sensitive to the out-of-plane magnetic moment of the transducer. TRMOKE experiments require the transducer's magnetic moment to point in the out-of-plane direction. If the magnetic moment does not point entirely in the out-of-plane direction, the TR-MOKE signal will not be entirely thermal in origin due to precessional effects [15]. Most magnetic thin films, e.g., Co or Fe, require external fields greater than 1 T to align the moment in the out-of-plane direction. It is experimentally challenging to apply a large out-of-plane magnetic moment, so it is desirable to use a transducer with large perpendicular magnetic anisotropy. This property makes it possible to align the moment in the out-of-plane direction with a weak field that can be supplied with a permanent magnet (< few hundred mT). Ferromagnetic multilayers with alternating sub-nm thick metal layers meet this criterion, e.g., Co/Pt, Co/Pd, CoFe/Pt, or Co/Ni. Rare-earth/transition-metal amorphous alloys, such as GdFeCo or TbFe [16,17] , are another option. Metals with large spin-orbit coupling typically have larger Kerr angles, and therefore better signal to noise ratio in TR-MOKE experiments. Additionally, metals with Curie temperatures that are not to high, e.g. 100-200 K above room temperature, also help with signal-to-noise by increasing dM/dT, and therefore the temperature-dependence of the Kerr angle.

TDTR without a metal transducer. While coating the sample with a thin metal film transducer offers advantages, it can also be a limitation. The transducer introduces an additional thermal boundary resistance at the metal/sample interface, which can reduce measurement sensitivities to the thermal properties of interest, such k of a high thermal conductivity material, k of a sub-surface

thin film, or G of buried interfaces [18]. The transducer can limit the temperature range over which a TDTR measurement can be conducted; most typical metal film transducers used in TDTR will either damage or react with the sample/environment, thus limiting TDTR measurements to an upper bound of around 1000 °C (this upper bound in temperature is strongly dependent on the type of metal film transducer used) [18–21]. To alleviate these potential limitations of using TDTR with a metal film transducer, it is thus promising to conduct TDTR measurements on materials without the metal film transducer, or a non-metal transducer that has higher temperature stability as compared to typical metals.

To this end, transducerless thermoreflectance techniques have been demonstrated for both bulk and thin film semiconductors [22–26]. However, as detailed by Wang *et al*. [22], there are additional experimental and modeling considerations that must be employed. In non-metals, the optical absorption depth is highly dependent on the photon energy relative to the bandgap energy. Non-metals are translucent or transparent to sub-bandgap energy photons, so above bandgap energies for pump and probe should be employed. Above bandgap energies ensure a shorter optical penetration depth. If the photon energy is high enough above the bandgap, the absorption depth can be metal-like, in which case a typical TDTR thermal analysis can be conducted; we note in this case for measurements on semi-infinite materials, only in-plane thermal diffusivity can be resolved with this typical analysis without a transducer [22]. However, without the use of UV sources, likely this scenario will not be the case, and thus the optical penetration depth of the pump and probe must be known and input into the analysis as a depth varying heat source, outlined in prior works.

One of the most important considerations in transducerless TDTR analysis in non-metals is the fact that the reflectivity change is highly dependent on both the temperature and carrier density[27–29]. If the pump changes the carrier density in the conduction or valence bands by exciting long-lived electron-hole pairs, then measured changes in reflectance will depend on both temperature and carrier density. Thermal properties can only be determined from temperature-induced changes in reflectance (thermoreflectance). Thus, carrier modulated changes to reflectance (often termed the “plasma” contribution to reflectivity) must be separated from the measured signals. An advantage of using TDTR to employ transducerless thermoreflectance measurements (as opposed to FDTR, for example), is that the plasma reflectance and thermoreflectance can be separated based

on pump-probe delay time and pump modulation frequency. If using an above bandgap pump, then the plasma component often decays faster than the thermal component, and this difference in decay time becomes more pronounced at lower modulation frequencies. Use of pump energies larger than the bandgap can help mitigate the effect of the plasma contribution to reflectivity by causing a faster decay of excited carriers (these criteria are reviewed by Salnick and Opsal) [27]. Thus, by conducting a transducerless TDTR measurement using above bandgap pump and probe energies at relatively low pump modulation frequencies, the majority of the measured change in reflectivity over the pump-probe delay time will be dominated by the thermoreflectance, as the plasma reflectivity component will be extinguished. Alternatively, the excited carrier contribution to reflectivity can be modeled [30]. This requires including a carrier diffusion equation that is coupled to the heat equation to analyze the data. This introduces additional parameters, and therefore can increase experimental uncertainties. However, if the electron dynamics of the excited non-metal are well known, in addition to the excited state optical properties at the pump and probe wavelengths, then the plasma vs. thermal contributions to the signal can be accurately modeled.

The above discussion focused on understanding the electronic absorption properties to conduct tranducerless TDTR, where the photon energies of the pump and probe should be as much above bandgap as possible to reduce the absorption depth and decrease the excited carrier lifetimes (thus reducing the plasma reflectivity signals); in short, this would typically mean using higher energy visible or UV sources in TDTR. However, recent work has discussed the concept of phonon thermoreflectance [31], where the temperature dependence of the optical phonon modes in polar materials can be used as a thermoreflectance probes. In this case, transducerless TDTR could be conducted by tuning the photon energy of the pump and probe to these infrared active phonon modes. In this case, there is little-to-no free carrier excitation, and the resulting change in reflectance that is measured is a pure thermoreflectance signal (i.e., no plasma component). Recent work has demonstrated the ability to probe these IR-active phonon modes in a pump probe experiment on AlN, SiO_2 and h-BN [31,32]. As with above bandgap experiments, implementing this approach for transducerless TDTR would involve a more specialized laser system as opposed to the standard TDTR Ti:Sapp. Oscillators, specifically with additional OPAs and DFGs to achieve sufficient photon fluences at these mid-IR energies. Further, typical optical penetration depths of radiation at these optical phonon energies are 1-2 orders of magnitude larger than the ~10-20 nm skin depth of a metal [31]. Still, this IR-TDTR approach embracing phonon thermoreflectance offers

the opportunity to conduct transducerless TDTR on materials typically transparent to high energy visible or UV light, such as WBG/UWBG semiconductors and insulators.[89,90]

Supplementary Note 4: Error Analysis

In well-controlled TDTR experiments, thermal conductivity can often be determined with 5–10% uncertainty, but complexities such as thin films or multiple unknown parameters increase measurement errors significantly. In short, there are two requirements for TDTR to be accurate. First, it is necessary to only fit for two parameters per data set, and to confirm that those parameters affect the measured signals in significantly different ways. Second, all other model input parameters need to be accurately known. To quantify how uncertainties in model parameters affect the measured signal, researchers often use either sensitivity analysis or Monte Carlo methods. Sensitivity analysis involves calculating sensitivity parameters, defined as the logarithmic derivative of the ratio. The sensitivity parameter describes how fractional changes in a thermal parameter influence the TDTR signal at different delay times or modulation frequencies. Once calculated with the thermal model, the sensitivity parameters allow for estimates of systematic error propagation. Sensitivity plots also guide experimental design by helping researchers choose laser modulation frequencies and pump–probe geometries that reduce parameter overlap, thereby enhancing confidence in extracted values. Monte Carlo simulations offer another view of how systematic errors propagate in TDTR. In Monte Carlo analysis, researchers assign probability distributions to all relevant inputs, such as sample thickness, heat capacity, and transducer properties, and randomly sample from these distributions to generate many datasets. Each dataset is then fit to the TDTR model, yielding a distribution of best-fit parameters that captures the combined effect of all uncertainties. By examining the spread of this distribution, one obtains confidence intervals.

Supplementary Note 5: Spurious Signals

Spurious signals can cause systematic errors in TDTR experiments, because the accuracy of TDTR depends on matching a thermal model to the measured thermoreflectance signal. Any voltage measured by the lock-in that does not stem from the predicted thermal response is, by definition, a "spurious signal", and will compromise the accuracy of the results.

A major source of these spurious signals arises from coherent pickup in the RF lock-in amplifier. Because the driving signal for the electro-optic modulator (EOM) operates at relatively high voltages (175 V), it is common for there to be weak electromagnetic coupling between the drive circuit and the sensitive detection electronics. Since thermoreflectance signals are on the order of μV, even coupling on the level of 10^{-8} can be problematic.

One approach to reduce the effect of coherent pickup from the driver is to introduce an optical chopper in the pump or probe beam. By modulating the light at a few hundred hertz (i.e., $\pm f_{\text{chopper}}$ away from the EOM frequency), the experimental signal of interest shifts to frequencies that can be more cleanly isolated from the strong driver frequency. However, this approach requires a two-stage lock-in detection scheme. The RF lock-in is operated with a short time constant (to capture frequencies at both f_{mod} and $f_{\text{mod}} \pm f_{\text{chopper}}$). Then, the signals measured by the lock-in are sent to a second audio-frequency lock-in that demodulates at the chopper frequency. The more complicated detection scheme reduces the signal-to-noise ratio by about a factor of two.

Another straightforward step toward mitigating spurious coupling is the use of high-performance double-shielded coaxial cables. We have found that such cables (e.g., those manufactured by Pasternack) are significantly more effective at minimizing pickup than standard coax lines.

Spurious signals can also arise from the optical layout and characteristics of the sample itself. Any clipping of the pump or probe beam can turn small thermoelastic deformations in the sample into unintended intensity modulations at the photodiode, particularly if the beam is partially blocked or deflected. Ensuring a clear optical path by carefully checking the beam footprint as it reflects back from the sample, through the objective lens, to the collection optics, and finally to the detector, will help avoid such artifacts. Similarly, paying attention to the shape of the beams on the camera can alert TDTR users to problems with the beam alignment. Finally, care needs to be taken to

center the reflected beam on the detector, and to make sure the detector area is much larger than the beam size.

Misalignment in the pump–probe overlap or unintentional beam wander as a function of delay time can create errors, especially for measurements of high thermal conductivity materials. Tracking the absolute signals of both V_{in} and V_{out} can be an excellent diagnostic tool for detecting problems. The in-phase voltage is determined by the transducer's optical properties and typically remains similar for a given pump–probe power, regardless of the underlying sample. Unusual deviations in the magnitude of V_{in} may indicate issues with the sample transducer or the optical alignment. Likewise, V_{out} should only vary by about 15–20% over a few nanoseconds of delay, so shifts larger than ~30% often point to alignment problems, such as the delay stage being misaligned or the spot sizes drifting.

A rough surface can be a significant source of spurious signal. Scattered pump light is generally harmless for common two-tint or two-color measurements because it is blocked from reaching the detector by filters. Alternatively, diffuse scattering of the probe can be modulated by thermoelastic effects caused by pump heating [33–38]. Therefore, diffusely scattered probe light will produce non-thermoreflectance intensity fluctuations at f_{mod}. Since this is a thermoelastic effect, it is most problematic in films with large coefficients of thermal expansion. Rough surfaces can also lead to acoustic artifacts that introduce signal via piezo-reflectance of the transducer [39]. Typically, the specular reflectance needs to be at least 95%. In materials with a low coefficient of thermal expansion, e.g., Si or AlN, the specular reflectance can be lower. The specular reflectance is straight forward to measure by monitoring the DC voltage on the detector. Picosecond acoustic signals can serve as another window into surface quality: rough surfaces broaden the acoustic echoes, and significant loss or smearing of these echoes can signal excessive surface roughness and diffuse scattering.

Soft materials, or composites with low elastic moduli, can exhibit additional complexities in short-time data. Lateral stress within the metal transducer can relax via zero-order symmetric Lamb waves, shifting the transducer reflectivity in a manner that falls outside typical thermal diffusion dynamics [40]. These thermoelastic signals are often strongest within the first few hundred picoseconds of the measurement and then die out. When such artifacts are present, analyzing only longer delay data helps to mitigate the error caused by them.

Finally, a key assumption in standard TDTR thermal modeling is that all pump light is absorbed at the transducer surface and that the measured reflectance change is solely a function of temperature in that opaque metal layer. If the transducer is partially transparent or has non-negligible optical penetration by the pump, these assumptions break down. In principle, one can extend the model to include absorption profiles, interference effects, and the thermo-optic response of multiple layers. However, adding these parameters greatly increases the model's complexity and likelihood of parameter correlation. For reliable, straightforward measurements, we find that a metal transducer layer of at least 50 nm thickness is typically sufficient to maintain the standard TDTR assumptions.

Supplementary References:

(1) Hopkins, P. E.; Phinney, L. M.; Serrano, J. R.; Beechem, T. E. Effects of Surface Roughness and Oxide Layer on the Thermal Boundary Conductance at Aluminum/Silicon Interfaces. *Phys Rev B* **2010**, *82* (8), 085307. https://doi.org/10.1103/PhysRevB.82.085307.

(2) Angeles, F.; Sun, Q.; Ortiz, V. H.; Shi, J.; Li, C.; Wilson, R. B. Interfacial Thermal Transport in Spin Caloritronic Material Systems. *Phys Rev Mater* **2021**, *5* (11), 114403. https://doi.org/10.1103/PhysRevMaterials.5.114403.

(3) Kang, K.; Koh, Y. K.; Chiritescu, C.; Zheng, X.; Cahill, D. G. Two-Tint Pump-Probe Measurements Using a Femtosecond Laser Oscillator and Sharp-Edged Optical Filters. *Review of Scientific Instruments* **2008**, *79* (11). https://doi.org/10.1063/1.3020759.

(4) Gomez, M. J.; Liu, K.; Lee, J. G.; Wilson, R. B. High Sensitivity Pump–Probe Measurements of Magnetic, Thermal, and Acoustic Phenomena with a Spectrally Tunable Oscillator. *Review of Scientific Instruments* **2020**, *91* (2), 023905. https://doi.org/10.1063/1.5126121.

(5) Chen, T.; Song, S.; Shen, Y.; Zhang, K.; Jiang, P. Simultaneous Measurement of Thermal Conductivity and Heat Capacity across Diverse Materials Using the Square-Pulsed Source (SPS) Technique. *International Communications in Heat and Mass Transfer* **2024**, *158*, 107849. https://doi.org/10.1016/j.icheatmasstransfer.2024.107849.

(6) Cahill, D. G. Analysis of Heat Flow in Layered Structures for Time-Domain Thermoreflectance. *Review of Scientific Instruments* **2004**, *75* (12), 5119–5122. https://doi.org/10.1063/1.1819431.

(7) Wilson, R. B.; Apgar, B. A.; Martin, L. W.; Cahill, D. G. Thermoreflectance of Metal Transducers for Optical Pump-Probe Studies of Thermal Properties. *Opt Express* **2012**, *20* (27), 28829. https://doi.org/10.1364/OE.20.028829.

(8) Peng, W.; Wilson, R. B. Thermal Model for Time-Domain Thermoreflectance Experiments in a Laser-Flash Geometry. *J Appl Phys* **2022**, *131* (13), 134301. https://doi.org/10.1063/5.0082549.

(9) Wilson, R. B.; Apgar, B. A.; Hsieh, W.-P.; Martin, L. W.; Cahill, D. G. Thermal Conductance of Strongly Bonded Metal-Oxide Interfaces. *Phys Rev B* **2015**, *91* (11), 115414. https://doi.org/10.1103/PhysRevB.91.115414.

(10) Wang, Y.; Park, J. Y.; Koh, Y. K.; Cahill, D. G. Thermoreflectance of Metal Transducers for Time-Domain Thermoreflectance. *J Appl Phys* **2010**, *108*, 43507.

(11) Rosei, R.; Colavita, E.; Franciosi, A.; Weaver, J. H.; Peterson, D. T. Electronic Structure of the Bcc Transition Metals: Thermoreflectance Studies of Bulk V, Nb, Ta, and αTaH_x. *Phys Rev B* **1980**, *21* (8), 3152–3157. https://doi.org/10.1103/PhysRevB.21.3152.

(12) Aller, H. T.; Yu, X.; Wise, A.; Howell, R. S.; Gellman, A. J.; McGaughey, A. J. H.; Malen, J. A. Chemical Reactions Impede Thermal Transport Across Metal/β-Ga2O3 Interfaces. *Nano Lett* **2019**, *19* (12), 8533–8538. https://doi.org/10.1021/acs.nanolett.9b03017.

(13) Khan, S.; Angeles, F.; Wright, J.; Vishwakarma, S.; Ortiz, V. H.; Guzman, E.; Kargar, F.; Balandin, A. A.; Smith, D. J.; Jena, D.; Xing, H. G.; Wilson, R. Properties for Thermally Conductive Interfaces with Wide Band Gap Materials. *ACS Appl Mater Interfaces* **2022**, *14* (31), 36178–36188. https://doi.org/10.1021/acsami.2c01351.

(14) Garfinkel, M.; Tiemann, J. J.; Engeler, W. E. Piezoreflectivity of the Noble Metals. *Physical Review* **1966**, *148* (2), 695–706. https://doi.org/10.1103/PhysRev.148.695.

(15) Lattery, D. M.; Zhu, J.; Zhang, D.; Wang, J.-P.; Crowell, P. A.; Wang, X. Quantitative Analysis and Optimization of Magnetization Precession Initiated by Ultrafast Optical Pulses. *Appl Phys Lett* **2018**, *113* (16). https://doi.org/10.1063/1.5046683.

(16) Chen, J.-Y.; Zhu, J.; Zhang, D.; Lattery, D. M.; Li, M.; Wang, J.-P.; Wang, X. Time-Resolved Magneto-Optical Kerr Effect of Magnetic Thin Films for Ultrafast Thermal Characterization. *J Phys Chem Lett* **2016**, *7* (13), 2328–2332. https://doi.org/10.1021/acs.jpclett.6b00945.

(17) Feser, J. P.; Liu, J.; Cahill, D. G. Pump-Probe Measurements of the Thermal Conductivity Tensor for Materials Lacking in-Plane Symmetry. *Review of Scientific Instruments* **2014**, *85* (10). https://doi.org/10.1063/1.4897622.

(18) Pfeifer, T. W.; Schonfeld, H. B.; Scott, E. A.; Aller, H.; Graham, S.; Gaskins, J. T.; Olson, D. H.; Braun, J.; Hopkins, P. E. Limitations and Advances in Optical Thermometry: Nanoscale Resistances, Ultrahigh Thermal Conductivity, and Ultrahigh Temperatures. *Annu Rev Mater Res*.

(19) Khan, S.; Shi, X.; Feser, J.; Wilson, R. Thermal Conductance of Interfaces between Titanium Nitride and Group IV Semiconductors at High Temperatures. *Appl Phys Lett* **2024**, *125* (4). https://doi.org/10.1063/5.0220124.

(20) Milich, M.; Quiambao-Tomko, K.; Hossain, M. D.; Tomko, J.; Maria, J.-P.; Hopkins, P. E. Ablation Threshold and Temperature Dependent Thermal Conductivity of High Entropy Carbide Thin Films. *High Temperatures-High Pressures* **2023**, *52* (2), 151–164. https://doi.org/10.32908/hthp.v52.1343.

(21) Zheng, Q.; Mei, A. B.; Tuteja, M.; Sangiovanni, D. G.; Hultman, L.; Petrov, I.; Greene, J. E.; Cahill, D. G. Phonon and Electron Contributions to the Thermal Conductivity of VN_x Epitaxial Layers. *Phys Rev Mater* **2017**, *1* (6), 065002. https://doi.org/10.1103/PhysRevMaterials.1.065002.

(22) Wang, L.; Cheaito, R.; Braun, J. L.; Giri, A.; Hopkins, P. E. Thermal Conductivity Measurements of Non-Metals via Combined Time- and Frequency-Domain Thermoreflectance without a Metal Film Transducer. *Review of Scientific Instruments* **2016**, *87* (9). https://doi.org/10.1063/1.4962711.

(23) Yang, J.; Ziade, E.; Schmidt, A. J. Modeling Optical Absorption for Thermoreflectance Measurements. *J Appl Phys* **2016**, *119* (9). https://doi.org/10.1063/1.4943176.

(24) Khafizov, M.; Yablinsky, C.; Allen, T. R.; Hurley, D. H. Measurement of Thermal Conductivity in Proton Irradiated Silicon. *Nucl Instrum Methods Phys Res B* **2014**, *325*, 11–14. https://doi.org/10.1016/j.nimb.2014.02.003.

(25) Qian, X.; Ding, Z.; Shin, J.; Schmidt, A. J.; Chen, G. Accurate Measurement of In-Plane Thermal Conductivity of Layered Materials without Metal Film Transducer Using Frequency Domain Thermoreflectance. *Review of Scientific Instruments* **2020**, *91* (6). https://doi.org/10.1063/5.0003770.

(26) Pomeroy, J. W.; Simon, R. B.; Sun, H.; Francis, D.; Faili, F.; Twitchen, D. J.; Kuball, M. Contactless Thermal Boundary Resistance Measurement of GaN-on-Diamond Wafers. *IEEE Electron Device Letters* **2014**, *35* (10), 1007–1009. https://doi.org/10.1109/LED.2014.2350075.

(27) Salnick, A.; Opsal, J. Dynamics of the Plasma and Thermal Waves in Surface-Modified Semiconductors. *Review of Scientific Instruments* **2003**, *74*, 545–549.

(28) Christofides, C.; Vitkin, I. A.; Mandelis, A. Photothermal Reflectance Investigation of Processed Silicon. I. Room-Temperature Study of the Induced Damage and of the Annealing Kinetics of Defects in Ion-Implanted Wafers. *J Appl Phys* **1990**, *67* (6), 2815–2821. https://doi.org/10.1063/1.345449.

(29) Vitkin, I. A.; Christofides, C.; Mandelis, A. Photothermal Reflectance Investigation of Processed Silicon. II. Signal Generation and Lattice Temperature Dependence in Ion-Implanted and Amorphous Thin Layers. *J Appl Phys* **1990**, *67* (6), 2822–2830. https://doi.org/10.1063/1.345450.

(30) Tanaka, T.; Harata, A.; Sawada, T. Subpicosecond Surface-Restricted Carrier and Thermal Dynamics by Transient Reflectivity Measurements. *J Appl Phys* **1997**, *82* (8), 4033–4038. https://doi.org/10.1063/1.365713.

(31) Hutchins, W. D.; Zare, S.; Hirt, D.; Golightly, E.; Hopkins, P. E. Infrared Phonon Thermoreflectance in Polar Dielectrics. **2025**.

(32) Hutchins, W.; Tomko, J. A.; Hirt, D. M.; Zare, S.; Matson, J. R.; Diaz-Granados, K.; He, M.; Pfeifer, T.; Li, J.; Edgar, J.; Maria, J.-P.; Caldwell, J. D.; Hopkins, P. E. Ultrafast Evanescent Heat Transfer across Solid Interfaces via Hyperbolic Phonon Polaritons in Hexagonal Boron Nitride. **2024**.

(33) Losego, M. D.; Grady, M. E.; Sottos, N. R.; Cahill, D. G.; Braun, P. V. Effects of Chemical Bonding on Heat Transport across Interfaces. *Nat Mater* **2012**, *11* (6), 502–506. https://doi.org/10.1038/nmat3303.

(34) Zheng, X.; Cahill, D. G.; Zhao, J.-C. Effect of MeV Ion Irradiation on the Coefficient of Thermal Expansion of Fe--Ni Invar Alloys: A Combinatorial Study. *Acta Mater* **2010**, *58* (4), 1236–1241.

(35) Zheng, X.; Cahill, D. G.; Weaver, R.; Zhao, J.-C. Micron-Scale Measurements of the Coefficient of Thermal Expansion by Time-Domain Probe Beam Deflection. *J Appl Phys* **2008**, *104*, 73509.

(36) Tomko, J. A.; Olson, D. H.; Giri, A.; Gaskins, J. T.; Donovan, B. F.; O'Malley, S. M.; Hopkins, P. E. Nanoscale Wetting and Energy Transmission at Solid/Liquid Interfaces. *Langmuir* **2019**, *35* (6), 2106–2114.

(37) Sun, J.; Cheng, Z.; Liang, J.; Shigekawa, N.; Kawamura, K.; Uratani, H.; Sakaida, Y.; Cahill, D. G. Probe Beam Deflection Technique with Liquid Immersion for Fast Mapping of Thermal Conductance. *Appl Phys Lett* **2024**, *124* (4), 42201. https://doi.org/10.1063/5.0179581.

(38) Sun, J.; Lv, G.; Cahill, D. G. Frequency-Domain Probe Beam Deflection Method for Measurement of Thermal Conductivity of Materials on Micron Length Scale. *Review of Scientific Instruments* **2023**, *94* (1), 14903. https://doi.org/10.1063/5.0126717.

(39) Szwejkowski, C. J.; Creange, N. C.; Sun, K.; Giri, A.; Donovan, B. F.; Constantin, C.; Hopkins, P. E. Size Effects in the Thermal Conductivity of Gallium Oxide (β -Ga2O3) Films Grown via Open-Atmosphere Annealing of Gallium Nitride. *J Appl Phys* **2015**, *117* (8). https://doi.org/10.1063/1.4913601.

(40) Wang, X.; Ho, V.; Segalman, R. A.; Cahill, D. G. Thermal Conductivity of High-Modulus Polymer Fibers. *Macromolecules* **2013**, *46* (12), 4937–4943. https://doi.org/10.1021/ma400612y.